Thermoelectric properties of Sb_2Te_3 under pressure and uniaxial stress

T. Thonhauser,[1] T. J. Scheidemantel,[1] J. O. Sofo,[1,2] J. V. Badding,[2,3] and G. D. Mahan[1,2]
[1]*Department of Physics, The Pennsylvania State University, University Park, Pennsylvania 16802, USA*
[2]*Materials Research Institute, The Pennsylvania State University, University Park, Pennsylvania 16802, USA*
[3]*Department of Chemistry, The Pennsylvania State University, University Park, Pennsylvania 16802, USA*
(Received 14 March 2003; published 1 August 2003)

We present first-principles transport calculations for Sb_2Te_3 using the linearized-augmented plane-wave method and the relaxation time approximation. We considered the effects of hydrostatic pressure and uniaxial stress up to 4 GPa. Doping was included for electrons and holes at levels up to $10^{21}/cm^3$. The electrical conductivity, the Seebeck coefficient, and the power factor are derived from the calculated transport distribution. Our results for the electronic structure and the transport properties are in qualitative agreement with experiment. Furthermore, we predict a large increase in the power factor under applied uniaxial stress.

DOI: 10.1103/PhysRevB.68.085201 PACS number(s): 71.15.Mb, 72.15.Jf, 72.10.Bg

I. INTRODUCTION

Compounds of bismuth, antimony, and tellurium are the best thermoelectric materials known yet for applications at or below room temperature. These materials have been investigated and optimized intensively.[1–5] Much effort has also been made to discover new thermoelectric materials that exhibit even better properties.[6–9] Pressure tuning may provide a means to guide the search for improved thermoelectric materials.[10–13] At room temperature, pressure-tuned *p*-doped $Sb_{1.5}Bi_{0.5}Te_3$ at about 2 GPa exhibits a value of ZT that is at least double its value at ambient pressure.[14] Thereby, ZT is the product of the thermoelectric figure of merit, Z, and temperature T. This provides a ''proof of principle'' that ZT values higher than the current record of approximately 1 are possible. It is important to develop an understanding of the origin of this much improved ZT, which may provide valuable insight into the search for improved thermoelectric materials at ambient pressure.

The electronic structure of a material plays a dominant role in its transport properties. During the last decade *ab initio* band-structure calculations have been reported for antimony telluride, bismuth telluride, and other basic compounds.[10,15–17] However, the detailed contributions of specific features of the electronic structure to the transport properties remain undetermined. Just recently, a code has been developed in addition to the WIEN2K density functional code[18] that allows the calculation of transport coefficients by means of *ab initio* methods.[19,20] Motivated by the experimental observations of the doubling of ZT under pressure,[14] we calculated the transport properties of Sb_2Te_3 under pressure and uniaxial stress using this code. The material used in the experiment is an antimony-rich alloy of antimony telluride and bismuth telluride ($Sb_{1.5}Bi_{0.5}Te_3$). Calculations for this material would be preferable, since the alloy disorder is of importance for both the electrical and thermal conductivity. However, supercell calculations with WIEN2K are numerically very intense, especially if optical properties are considered. Therefore, we have calculated the electronic structure and transport properties for Sb_2Te_3. The alloy properties are likely to be between the properties of Sb_2Te_3 and Bi_2Te_3, but closer to those of Sb_2Te_3. Nevertheless, supercell calculations of the alloy might be practical in the near future.

Our calculations provide detailed information about the relationship between the changes in the electronic structure and the changes in the transport coefficients induced by pressure. Furthermore, we find that under uniaxial stress Sb_2Te_3 metallizes at much lower pressures than under hydrostatic stress and that the Seebeck coefficient for this metalized semiconductor is much higher than typically observed for metals.

II. THEORY

The group velocity $\vec{v}$, which is the derivative of the band energy ϵ_k with respect to the wave vector, is a key quantity for the calculation of transport properties and is often evaluated numerically. If the expression for $\vec{v}$ is rewritten to include the momentum operator $\vec{p}$,

$$\vec{v}_k = \frac{1}{\hbar}\frac{\partial \epsilon_k}{\partial \vec{k}} = \frac{1}{m}\langle k|\vec{p}\,|k\rangle = \frac{1}{m}\vec{p}_k, \tag{2.1}$$

transport properties can be calculated by *ab initio* methods. Here, $\vec{k}$ is a wave vector, $|k\rangle$ is the corresponding electronic state, and m stands for the electron mass. The details of this approach can be found in Refs. 19 and 20. The matrix element in Eq. (2.1) is called the *optical matrix element* and is implemented in the WIEN2K code within the optic package.[21] Once this matrix element is known, transport properties such as the Seebeck coefficient $\boldsymbol{S}$, the electrical conductivity $\boldsymbol{\sigma}$, and the electronic part of the thermal conductivity, $\boldsymbol{\kappa}_{\mathrm{el}} = \boldsymbol{\kappa}_0 - T\boldsymbol{\sigma}\boldsymbol{S}\boldsymbol{S}$, can be calculated:

$$\boldsymbol{\sigma} = e^2 \sum_k \left(-\frac{\partial f_0}{\partial \epsilon}\right) \tau_k \vec{v}_k \vec{v}_k, \tag{2.2}$$

$$\boldsymbol{S} = e k_B \boldsymbol{\sigma}^{-1} \sum_k \left(-\frac{\partial f_0}{\partial \epsilon}\right) \tau_k \vec{v}_k \vec{v}_k \frac{\epsilon_k - \mu}{k_B T}, \tag{2.3}$$

$$\boldsymbol{\kappa}_0 = k_B^2 T \sum_k \left(-\frac{\partial f_0}{\partial \epsilon}\right) \tau_k \vec{v}_k \vec{v}_k \left[\frac{\epsilon_k - \mu}{k_B T}\right]^2. \tag{2.4}$$

Here, τ_k and f_0 denote the relaxation time and the Fermi function, respectively; e denotes the electronic charge, k_B Boltzmann's constant, μ the chemical potential, and T the temperature.

Several approximations for the scattering are possible; however, the *relaxation time approximation* is most commonly used. Within this framework further approximations can be made; the simplest one assumes constant τ. This is reasonable for transport properties since they include the derivative of the Fermi function. The magnitude of this derivative is significant only within a small energy window of about $10k_BT$ (e.g., ~ 0.26 eV for $T=300$ K) near the Fermi energy and most likely τ does not vary much over this interval. However, we should keep in mind that this approach neglects dependences of the relaxation time on quantities such as momentum, position, or the band index.

All the material-dependent properties in Eqs. (2.2)–(2.4) can be combined to give the so-called transport distribution $\boldsymbol{\Xi}(\epsilon)$ (Ref. 22):

$$\boldsymbol{\Xi}(\epsilon)=\sum_k \tau_k \ \vec{v}_k\vec{v}_k \ \delta(\epsilon-\epsilon_k), \tag{2.5}$$

where $\delta(\epsilon-\epsilon_k)$ denotes the delta function. Transport coefficients such as $\boldsymbol{S}$, $\boldsymbol{\sigma}$, and $\boldsymbol{\kappa}_{\mathrm{el}}$ can then be derived from the material-dependent transport distribution by performing material-independent operations. $\boldsymbol{\Xi}(\epsilon)$ contains all of the intrinsic information about the materials transport properties and is therefore the quantity of interest.

Now, all transport coefficients can be rewritten to include the transport distribution. Using an integral over the energy instead of a $\vec{k}$-point sum, Eqs. (2.2)–(2.4) become

$$\boldsymbol{\sigma}= \quad e^2\int d\epsilon \ \left(-\frac{\partial f_0}{\partial\epsilon}\right) \ \boldsymbol{\Xi}(\epsilon), \tag{2.6}$$

$$\boldsymbol{S}=ek_B \ \boldsymbol{\sigma}^{-1}\int d\epsilon \ \left(-\frac{\partial f_0}{\partial\epsilon}\right) \ \boldsymbol{\Xi}(\epsilon) \ \frac{\epsilon-\mu}{k_BT}, \tag{2.7}$$

$$\boldsymbol{\kappa}_0= \quad k_B^2T\int d\epsilon \ \left(-\frac{\partial f_0}{\partial\epsilon}\right) \ \boldsymbol{\Xi}(\epsilon) \ \left[\frac{\epsilon-\mu}{k_BT}\right]^2. \tag{2.8}$$

For the analysis of the Seebeck coefficient it is convenient to introduce the quantity

$$\aleph=ek_B\int d\epsilon \ \left(-\frac{\partial f_0}{\partial\epsilon}\right) \ \boldsymbol{\Xi}(\epsilon) \ \frac{\epsilon-\mu}{k_BT}, \tag{2.9}$$

since it includes the same integral as the Seebeck coefficient; however, it does not include $\boldsymbol{\sigma}$.

III. COMPUTATIONAL DETAILS

We used the rhombohedral setting for the unit cell of Sb_2Te_3, which has three inequivalent atoms per cell and five atoms in total. This material crystallizes in a five-layer structure (Te-Sb-Te-Sb-Te) within the D_{3d}^5 $(R\bar{3}m)$ space group. For convenience the hexagonal unit cell with lattice parameters a and c is often used. Pictorial representations of the crystal structure and the first Brillouin zone can be found in Ref. 15.

All calculations were performed within the full-potential linearized-augmented plane-wave (FP-LAPW) method as implemented in the WIEN2K code.[18] Here 1083 basis functions were used, corresponding to a $RK_{\max}$ value of 10, where the muffin-tin radii have been chosen to be 2.7 a.u. for Sb and Te. The potentials and charge densities were represented by 13 404 stars in the interstitial region and by spherical harmonics up to $L=6$ within the muffin-tin spheres. For Brillouin-zone (BZ) integrations, 1000 $\vec{k}$ points within the whole BZ were used during the self-consistency cycle. Convergence tests for the transport properties showed that at least 75 000 $\vec{k}$ points in the entire BZ had to be included when the optical matrix elements are calculated. Exchange and correlation effects were accounted for by the generalized gradient approximation parametrized by Perdew, Burke, and Ernzerhof.[23] Spin-orbit coupling was included, except for the calculation of the atomic forces and relaxation of the atomic positions.

A constant relaxation time τ was used for all calculations of transport properties. It follows from Eqs. (2.5) and (2.7) that for this particular choice of τ the Seebeck coefficient is independent of the relaxation time and thus the scattering mechanism. Doping was treated within the rigid-band approximation and the temperature dependence of the band structure was neglected.

IV. RESULTS AND DISCUSSION

A. Total energy and band structure

Starting from the experimental values,[24] we determined the total energy for 312 different values of the hexagonal lattice parameters a and c. For each point the atomic forces were relaxed. The resulting energy surface was then fitted to third-order polynomials of the lattice parameters. From this fit, we determined the values for hydrostatic pressure and uniaxial stress in terms of the hexagonal a and c lattice parameters.

The hydrostatic pressure was found to increase linearly with decreasing volume over the region of interest. For structures under uniaxial stress, a force was applied to shrink the hexagonal c lattice parameter and thereby letting the a lattice parameter relax i. e., expand. Uniaxial stress, volume, and a depend linearly on c in the region of interest. Numerical values for a and c, as well as the relative atom positions for Sb and Te under pressure and uniaxial stress, are given in Table I.

We also calculated energies along a commonly used path in the BZ that includes the maximum of the valence band and the minimum of the conduction band. Figure 1 displays the band structure for Sb_2Te_3 with and without spin-orbit coupling. The results show that spin-orbit coupling is indeed necessary to describe the material correctly. Without spin orbit coupling a direct band gap is found at Γ. By including spin-orbit coupling the valence-band maximum is found at a non-high-symmetry point along the line Γ-a and the conduction band minimum occurs along the line Γ-Z, in agreement

TABLE I. Hexagonal lattice parameters a and c in a.u., as well as relative atom positions of Te and Sb, under pressure and uniaxial stress in GPa. The corresponding experimental values at ambient pressure are (Ref. 24) $a=8.0578$ a.u., $b=57.5573$ a.u., Sb position $=0.3988$, and Te position$=0.7869$.

Pressure		0.0	1.0	2.0	3.0	4.0
Hydrostatic	a	8.2199	8.1644	8.1123	8.0630	8.0162
	c	58.287	57.893	57.524	57.174	56.842
	Sb	0.3977	0.3982	0.3987	0.3990	0.3993
	Te	0.7864	0.7876	0.7887	0.7895	0.7903
Uniaxial	a	8.2199	8.2885	8.3620	8.4412	8.5265
	c	58.287	56.981	55.649	54.286	52.887
	Sb	0.3977	0.3985	0.3987	0.3994	0.3998
	Te	0.7864	0.7879	0.7886	0.7897	0.7908

with Ref. 10. This multivalley band structure, which is responsible for the excellent thermoelectric properties, is a result of spin-orbit coupling. If these relativistic effects are neglected, a single-valley valence-band maximum and a single-valley conduction-band minimum, occurring at Γ, are found.

The band structure at 0 and 4 GPa of applied uniaxial stress is shown in Fig. 2. As a result of the large changes in the band structure under pressure, large changes in the transport properties can be expected.

B. Density of states

We also calculated the behavior of the density of states (DOS) under pressure and uniaxial stress, and the results are depicted in Fig. 3. In general, for hydrostatic pressure, the overall change in the DOS is a small shift toward lower energies. Uniaxial stress, however, produces a redistribution of the electronic states, which brings more states from lower energies closer to the Fermi energy. The peak in the DOS at around -0.6 eV for 0 GPa vanishes in favor of a higher density of states around -0.2 eV for higher stress. This corresponds to changes along several lines in the band structure depicted in Fig. 2 and is most obvious along the lines Γ-L and U-a. Furthermore, bands crossing the Fermi energy are present after metalization occurs at 2.5 GPa.

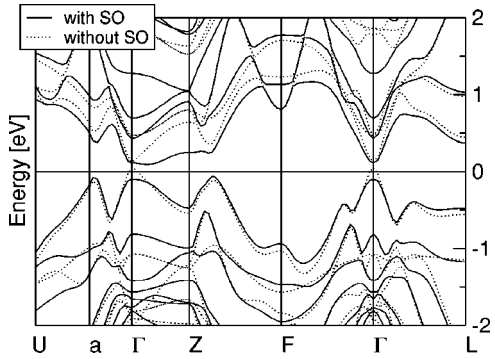

FIG. 1. Band structure of Sb_2Te_3 with and without spin-orbit (SO) coupling.

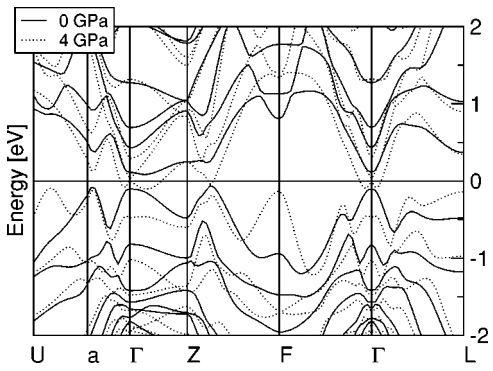

FIG. 2. Band structure of Sb_2Te_3 under 0 and 4 GPa of uniaxial stress.

The energy gap calculated from the DOS is 0.278 eV at zero pressure, which is in excellent agreement with the published value of 0.28 eV.[25] However, in consideration of the usual underestimation of energy gaps calculated with the generalized gradient approximation, it is possible that the match is coincidental. As a result of the general shift of the DOS, the gap changes little under hydrostatic pressure. This is in contrast to the case of uniaxial stress, where the band gap decreases with increasing stress so that at about 2.5 GPa metalization occurs, supporting the idea of Itskevich and co-workers.[12,13]

C. Transport distribution

The DOS provides the energies of electronic states, but does not provide any information about how these states contribute to the electronic transport. We calculated the transport distribution as defined in Eq. (2.5) for a range of values of applied pressure and uniaxial stress. Results for the xx and zz component are shown in Fig. 4 over a wide range of energy. For symmetry reasons the yy component is equivalent to the xx component. The anisotropy of the material is evident from the transport distribution, information that cannot be extracted from the DOS. The DOS counts all the

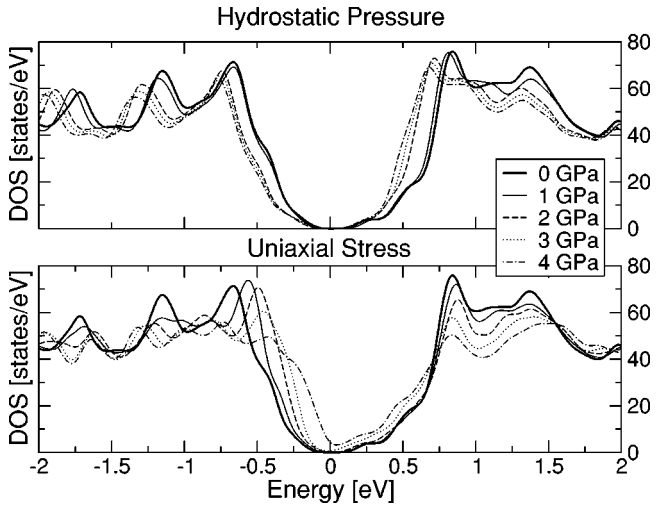

FIG. 3. DOS of Sb_2Te_3 for 0 up to 4 GPa. The energy is plotted with respect to the Fermi energy.

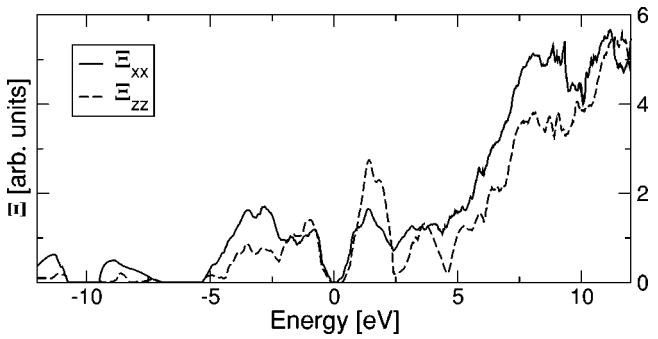

FIG. 4. *xx* and *zz* component of the transport distribution $\Xi(\epsilon)$ for Sb_2Te_3 under the assumption of constant relaxation time τ. Here $\Xi(\epsilon)$ is given in arbitrary units and the energy is given with respect to the Fermi energy.

states available at a certain energy, while $\Xi(\epsilon)$ includes only those states that contribute in a significant way to the transport process in a given direction.

The top graphs of Figs. 5 and 6 show $\Xi(\epsilon)$ for several

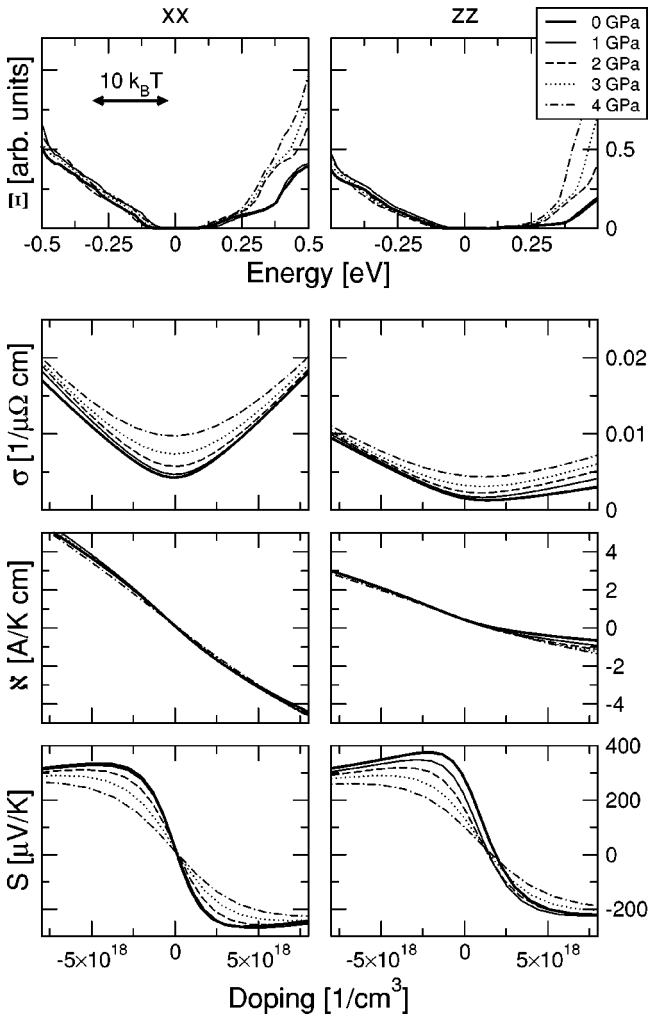

FIG. 5. *xx* and *zz* component of $\Xi(\epsilon)$, $\boldsymbol{\sigma}$, $\aleph$, and $\boldsymbol{S}$ for Sb_2Te_3 under 0–4 GPa of hydrostatic pressure and $T=300$ K. Negative doping concentrations denote hole doping. The value of $10k_BT$ for room temperature is depicted for reference.

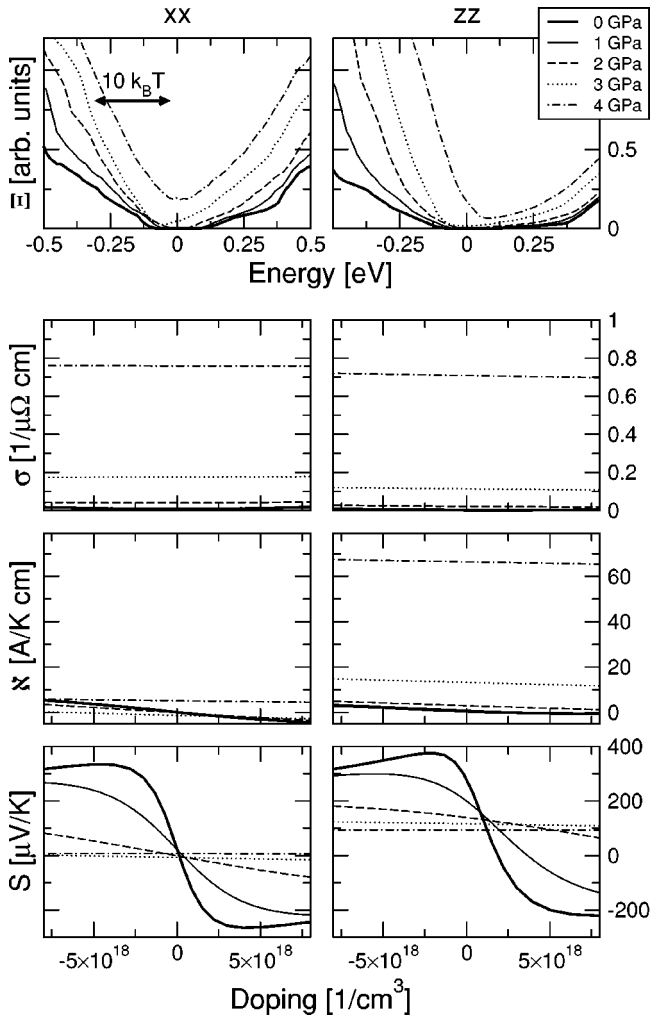

FIG. 6. *xx* and *zz* component of $\Xi(\epsilon)$, $\boldsymbol{\sigma}$, $\aleph$, and $\boldsymbol{S}$ for Sb_2Te_3 under 0–4 GPa of uniaxial stress and $T=300$ K. Negative doping concentrations denote hole doping. The value of $10k_BT$ for room temperature is depicted for reference.

different values of pressure and stress. In general, in all cases the valley structure of $\Xi(\epsilon)$ steepens around the Fermi energy. However, under uniaxial stress there are steeper slopes at positive and negative energies, whereas in the case of hydrostatic pressure only the slope for positive energies increases. These observations can be connected to the change in the DOS, as mentioned above. In particular, note the similarity of the *zz* component of $\Xi(\epsilon)$ and the DOS for uniaxial stress. This is a result of the shrinking of the *c* axis under uniaxial stress.

D. Electrical conductivity

The electrical conductivity can be readily derived from the transport distribution. We calculated $\boldsymbol{\sigma}$ for a wide range of values of the chemical potential μ corresponding to various doping levels. Results for a temperature of 300 K are plotted in Figs. 5 and 6. The relaxation time was fitted to 1.082×10^{-12} sec, so that the intrinsic *xx* component of the conductivity for ambient pressure and zero doping equals the experimental value.[25] Note that the calculated *zz* component

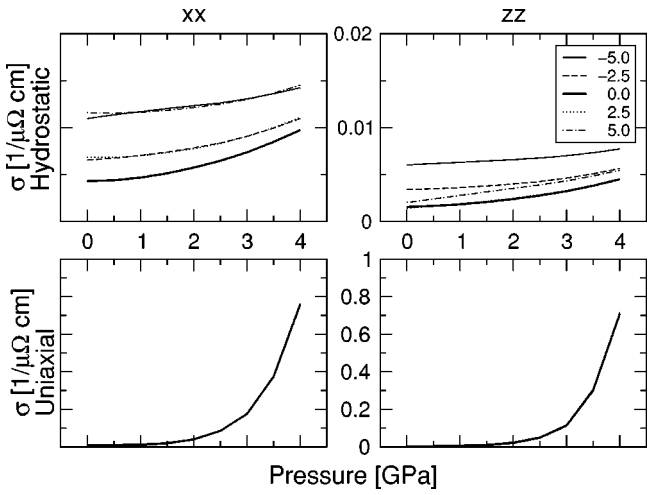

FIG. 7. *xx* and *zz* component of $\boldsymbol{\sigma}$ for Sb_2Te_3 under pressure. The curves correspond to different doping levels given in units of $10^{18}/cm^3$. Under uniaxial stress the curves are almost indistinguishable.

for these conditions exactly matches the experimental value, which illustrates the reliability of the code used.

According to Eq. (2.6), $\boldsymbol{\sigma}$ is the integral over the transport distribution multiplied by the derivative of the Fermi function. Since $\Xi(\epsilon)$ generally increases under pressure, the conductivity shows the same effect. Note that both negative and positive energies, with respect to the chemical potential, contribute toward the increase of conductivity because the derivative of the Fermi function is a symmetric function. The doping behavior of $\boldsymbol{\sigma}$ can also be understood with the help of its integral definition: By shifting the chemical potential to either the left or right of the Fermi energy, the area under the transport distribution increases. Thus, the conductivity increases, in accordance with the physical picture of doping and conductivity.

There are significant differences between the conductivity in the Sb_2Te_3 planes and perpendicular to the them, as well as under hydrostatic pressure and uniaxial stress. It can be seen that, in general, the conductivity in the planes is larger than the conductivity perpendicular to them, in agreement with experiment.[25] Note that $\boldsymbol{\sigma}$ in the *zz* direction under hydrostatic pressure does not have its minimum for the intrinsic material. This is evident from the asymmetry of the transport distribution around the Fermi energy. Further, note that the conductivity under uniaxial stress is much larger than under hydrostatic pressure. This difference in the conductivities can directly be seen from $\Xi(\epsilon)$ and results from the metallization under uniaxial stress. Also, as expected for a metal, the relative variation of $\boldsymbol{\sigma}$ with doping becomes smaller as the uniaxial stress increases. The range for the chemical potential necessary to produce the same doping range becomes smaller under uniaxial stress i.e., as the material becomes more metallic.

We determined the conductivity under pressure and stress for five different doping concentrations (Fig. 7). As previously discussed, $\boldsymbol{\sigma}$ always increases under pressure. In this representation, the strong increase of conductivity and its independence of doping under uniaxial stress can be seen more clearly.

The increase of conductivity is in agreement with experiment; however, to compare our results, it is important to understand the experimental setup as described in Ref. 14. The experiments were performed on polycrystalline sections of $Sb_{1.5}Bi_{0.5}Te_3$ compressed in a diamond anvil cell surrounded with monoclinic ZrO_2. A substantial uniaxial stress component is induced by this nonhydrostatic medium. Therefore, the experiments represent an average over various crystallographic directions and stress components. The experimental maximum in the thermoelectric power appears to correlate with the pressure at which the ZrO_2 medium likely begins to flow and therefore decreases the uniaxial stress component. Thus, it is experimentally observed that the details of the stress components have a large impact on the thermoelectric power and conductivity.

E. Seebeck coefficient

We also calculated the Seebeck coefficient from the transport distribution. Results for the *xx* and *zz* component at 300 K are plotted at various doping levels in the bottom graphs of Figs. 5 and 6. In accordance to reported values,[2] the *zz* component is, in general, somewhat larger than the *xx* component. It can also be seen that the Seebeck coefficient in almost all cases decreases under pressure. Furthermore, the decrease under uniaxial stress is much more pronounced than under hydrostatic pressure.

The behavior of the Seebeck coefficient can be understood better by looking at the quantity $\aleph$ as defined in Eq. (2.9). Like the conductivity, $\aleph$ is an integral over the transport distribution multiplied by the derivative of the Fermi function. However, in addition the integrand is multiplied by the term $(\epsilon-\mu)$, which is an asymmetric function. Thus, contributions of the transport distribution from negative and positive energies with respect to μ can cancel each other, in contradiction to the conductivity, where they always contribute with the same sign. We have plotted $\aleph$ in Figs. 5 and 6.

For hydrostatic pressure $\aleph$ almost does not vary under pressure, which is a result of the canceling mentioned above. The behavior of the Seebeck coefficient now follows naturally by calculating it as $S=\aleph/\sigma$ for each component. It is obvious that the decrease in the Seebeck under hydrostatic pressure originates mostly in the increase of the conductivity. It also follows that the Seebeck coefficient in the *zz* direction has a nonzero value for the intrinsic material, since the zero crossing of $\aleph$ is not at zero doping.

The situation is similar for applied uniaxial stress. For the *xx* direction, the large increase of conductivity explains the large decrease of the Seebeck under pressure because $\aleph$ does not increase enough to counteract this trend. This is evident from the transport distribution, which is rather symmetric with respect to the Fermi energy. For the *zz* direction, however, $\aleph$ changes on a much bigger scale compared to the *xx* direction, which can directly be related to the asymmetry of $\Xi(\epsilon)$ around the Fermi energy. It is interesting to see that under uniaxial stress the conductivity increases as expected

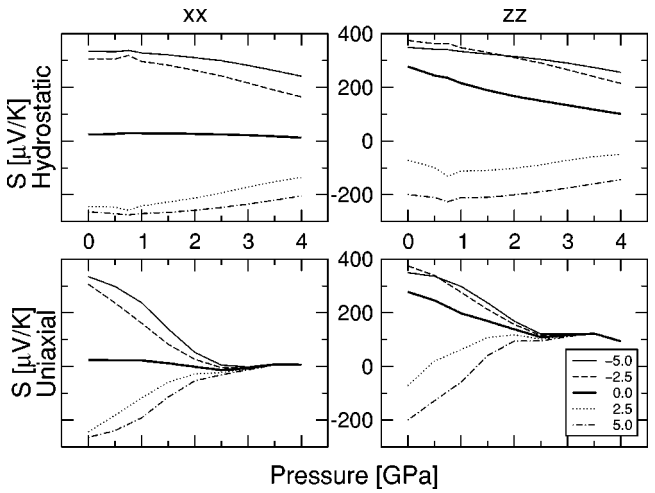

FIG. 8. *xx* and *zz* component of $\boldsymbol{S}$ for Sb_2Te_3 under pressure. The curves correspond to different doping levels given in units of $10^{18}/cm^3$.

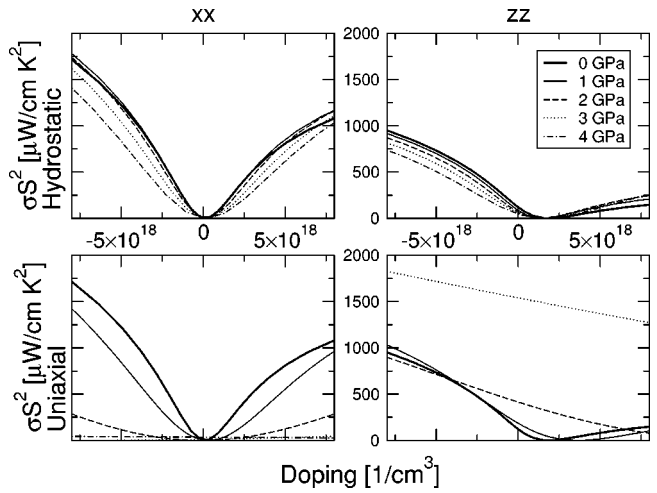

FIG. 9. *xx* and *zz* component of σS^2 for Sb_2Te_3 under 0–4 GPa. Curves are depicted for a temperature of 300 K.

during metallization; however, a not-negligible Seebeck coefficient remains, which is not typical for metals. The special change in the transport distribution under stress makes this possible. $\Xi(\epsilon)$ increases for negative energies due to an increased DOS, as can be seen in Fig. 3. However, at the same time $\vec{v}\cdot\vec{v}$ does not decrease. For positive energies, the change with stress is much smaller; thus $\Xi(\epsilon)$ becomes more and more asymmetric. The combination of these two effects results in a transport distribution that allows a relatively high Seebeck coefficient for a metal.

Figure 8 gives the Seebeck coefficient plotted over pressure for different doping concentrations. The general decrease of $\boldsymbol{S}$ with pressure is obvious. Additional points were inserted between zero and 1 GPa and small peaks show up at about 0.75 GPa, most pronounced for a doping of 2.5 $\times 10^{18}/cm^3$ in the *zz* direction. It can also be seen that uniaxial stress can change the type of the thermoelectric material in the *zz* direction making an *n*-type thermoelectric out of a *p*-type one.

F. Power factor

From the data for the electrical conductivity and the Seebeck coefficient the power factor σS^2 can be calculated. Results for the *xx* and *zz* component at 300 K are plotted versus the doping level in Fig. 9. Results for the power factor versus pressure and stress are depicted in Fig. 10.

The metallization observed under uniaxial stress at 2.5 GPa produces a redistribution of the electronic states bringing more states from lower energies closer to the Fermi level as can be seen in the DOS in Fig. 3. These new states closer to the Fermi level have a group velocity that is not diminished because of the reordering, offering an important contribution to the conductivity and still maintaining a reasonable value for the Seebeck coefficient. As a result, we can see in Fig. 10 a big increase of the power factor in the *zz* direction. This is not the case for the in-plane direction where the increase of the DOS is counterbalanced by a decrease in the group velocity, keeping a fairly symmetric shape of the transport distribution around the Fermi level.

V. CONCLUSIONS

The transport coefficients of Sb_2Te_3 show a rich behavior under pressure. Using a combination of first-principles electronic structure calculations and the relaxation time approximation we obtained a theoretical evaluation of the coefficients that is relevant for thermoelectric applications. The transport properties are strongly dependent on the type of stress applied to Sb_2Te_3. While hydrostatic pressure has a modest effect on the transport coefficients, uniaxial stress applied perpendicular to the planes of the layered structure substantially improves the power factor of the material. The system becomes semimetallic while the transport distribution remains asymmetric near the Fermi level. As a result, the electrical conductivity becomes larger while the Seebeck coefficient remains substantial, which is unusual, since higher

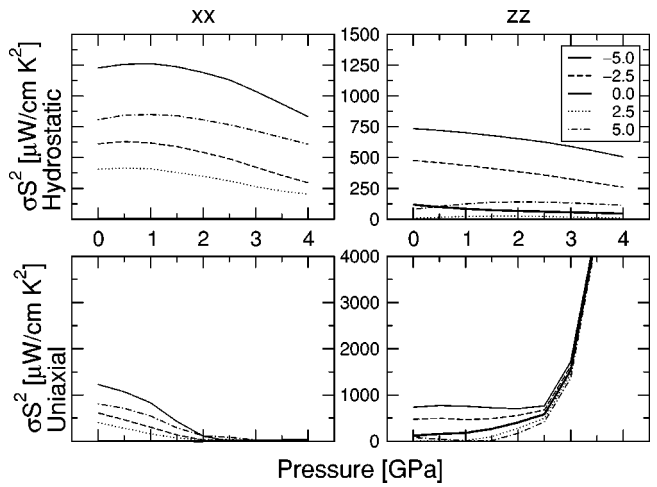

FIG. 10. *xx* and *zz* component of the power factor for Sb_2Te_3 under pressure. The curves correspond to different doping levels given in units of $10^{18}/cm^3$.

electrical conductivity usually corresponds to a lower Seebeck coefficient and therefore to a decrease in the device performance. However, the device performance is also influenced by the thermal conductivity, which is the sum of two parts: the electronic contribution to the thermal conductivity and the lattice thermal conductivity. Accordingly to the Wiedemann-Franz law, along with the increase in the electrical conductivity there will be a proportional increase in the electronic contribution to the thermal conductivity, which, in turn, decreases the device performance. The change of the lattice thermal conductivity under stress cannot be predicted within our *ab initio* method. Therefore, although the power factor becomes larger under uniaxial stress, the thermoelectric figure of merit may not increase.

In our analysis we stress the importance of using the transport distribution to study the effects of electronic structure on transport coefficients. The density of states provides information on the energy distribution of the states. It lacks, however, any information on the contribution of these states to the transport. This is evident from the differences in the xx and zz components of $\boldsymbol{\sigma}$, $\boldsymbol{S}$, and σS^2. Here $\boldsymbol{\Xi}(\epsilon)$ accounts for the directional dependence of the group velocity and is therefore the quantity of interest.

Perhaps the most significant conclusion from our calculations is that it is possible to have a large Seebeck coefficient together with metalliclike conductivities for a semiconductor such as Sb_2Te_3. It has not, in general, been realized that such high values for the Seebeck coefficient are possible for semiconductors near an insulator-metal transition that have such high values for the electrical conductivity. Significant stresses and pressures can be ''locked in'' to suitably nanostructured or microstructured materials that can be utilized at ambient pressure.[26,27] Such an approach might allow for stress tuning of Sb_2Te_3 and its alloys to improve their thermoelectric properties. Ghoshal *et al.* find that there is enhanced thermoelectric cooling at cold junction interfaces that likely have a substantial uniaxial stress component.[28] Our results may also inspire efforts to chemically tune semiconductors to reproduce the calculated power factors.

In view of the differences between the stress conditions of the present calculations and the experiments in the diamond anvil cell, the changes in the transport coefficients under stress are in qualitative agreement with experiment. The experiments were done on polycrystalline alloys, and the stress conditions were neither purely uniaxial nor hydrostatic. Stress applied to different crystallographic orientations will likely give rise to very different changes in the transport behavior. It would be valuable to perform transport measurements on oriented single crystals of pure antimony telluride and antimony bismuth telluride alloy for comparison with the present calculations as well as calculations on different crystallographic orientations.

ACKNOWLEDGMENTS

This work was funded by NFS Grant No. DMR-02-05125. Furthermore, it was supported in part by the Materials Simulation Center, a Penn-State MRSEC and MRI facility.

[1] D. M. Rowe, *CRC Handbook of Thermoelectrics* (CRC Press, Boca Raton, 1995).
[2] H. J. Goldsmid, *Electronic Refrigeration*, (Pion, London, 1986).
[3] G. D. Mahan, Solid State Phys. **51**, 81 (1998).
[4] F. J. DiSalvo, Science **285**, 703 (1999).
[5] T. M. Tritt, Science **283**, 804 (1999).
[6] G. A. Slack and V. G. Tsoukala, J. Appl. Phys. **76**, 1665 (1994).
[7] D. J. Singh and W. E. Pickett, Phys. Rev. B **50**, 11 235 (1994).
[8] B. C. Sales, D. Mandrus, and R. K. Williams, Science **272**, 1325 (1996).
[9] M. G. Kanatzidis, in *Recent Trends in Thermoelectric Materials Research I*, edited T. Tritt (Academic Press, San Diego, 2001), Vol. 69, p. 515.
[10] M. Bartkowiak and G. D. Mahan, in *Proceedings of the 18th International Conference on Thermoelectrics*, (IEEE, Piscataway, NJ, 1999), p. 71.
[11] C. D. W. Jones, K. A. Regan, and F. J. DiSalvo, Phys. Rev. B **58**, 16 057 (1998).
[12] E. S. Itskevich, L. M. Kashirskaya, and V. F. Kraidenov, Semiconductors **31**, 276 (1996).
[13] V. V. Sologub, M. L. Shubnikov, E. S. Itskevich, L. M. Kashirskaya, R. V. Parfen'ev, and A. D. Goletskaya, Sov. Phys. JETP **52**, 1203 (1980).
[14] D. A. Polvani, J. F. Meng, N. V. Chandra Shekar, J. Sharp, and J. V. Badding, Chem. Mater. **13**, 2068 (2001).
[15] S. K. Mishra, S. Satpathy, and O. Jepsen, J. Phys.: Condens. Matter **9**, 461 (1997).
[16] G. A. Thomas, D. H. Rapkine, R. B. van Dover, L. F. Mattheiss, W. A. Sunder, L. F. Schneemeyer, and J. V. Waszczak, Phys. Rev. B **46**, 1553 (1992).
[17] D. J. Singh, in *Recent Trends in Thermoelectric Materials Research II*, edited T. Tritt (Academic Press, San Diego, 2001), Vol. 70, p. 125.
[18] P. Blaha, K. Schwarz, G. K. H. Madsen, D. Kvasnicka, and J. Luitz, K. Schwarz, computer code WIEN2K, An Augmented Plane Wave + Local Orbitals Programm for Calculating Crystal Properties, Technical Universität Wien, Austria, 2001.
[19] T. J. Scheidemantel and J. O. Sofo, in *Chemistry, Physics and Materials Science of Thermoelectric Materials: Beyond Bismuth Telluride*, edited by M. G. Kanatzidis, T. P. Hogan, and S. D. Mahanti (Kluwer Academic/Plenum, New York, 2003).
[20] T. J. Scheidemantel, T. Thonhauser, J. V. Badding, and J. O. Sofo (unpublished).
[21] C. Ambrosch-Draxl and J. O. Sofo (unpublished).
[22] G. D. Mahan and J. O. Sofo, Proc. Natl. Acad. Sci. U.S.A. **93**, 7436 (1996).
[23] J. P. Perdew, K. Burke, and M. Ernzerhof, Phys. Rev. Lett. **77**, 3865 (1996).
[24] P. Villars and L. D. Calvert, *Pearson's Handbook of Crystallographic Data for Intermetallic Phases*, 2nd ed. (ASM International, Materials Park, OH 1991).

[25] *Numerical Data and Functional Relationships in Science and Technology*, Landolt-Börnstein, New Series, Group III, Vol. 17, pt.f, edited by O. Madelung, M. Schulz, and H. Weiss (Springer, New York, 1983).
[26] J.-P. Locquet, J. Perret, J. Fompeyrine, E. Mächler, J. W. Seo, and G. Van Tendeloo, Nature (London) **394**, 453 (1998).
[27] J. V. Badding, Annu. Rev. Mater. Sci. **28**, 631 (1998).
[28] U. Ghoshal, S. Ghoshal, C. McDowell, L. Shi, S. Cordes, and M. Farinelli, Appl. Phys. Lett. **80**, 3006 (2002).